Portable Remote Imaging Spectrometer coastal ocean sensor: design, characteristics, and first flight results

Pantazis Mouroulis,[1,*] Byron Van Gorp,[1] Robert O. Green,[1] Heidi Dierssen,[2]
Daniel W. Wilson,[1] Michael Eastwood,[1] Joseph Boardman,[3] Bo-Cai Gao,[4]
David Cohen,[1] Brian Franklin,[1] Frank Loya,[1] Sarah Lundeen,[1]
Alan Mazer,[1] Ian McCubbin,[5] David Randall,[1] Brandon Richardson,[1]
Jose I. Rodriguez,[1] Charles Sarture,[1] Eugenio Urquiza,[1]
Rudolph Vargas,[1] Victor White,[1] and Karl Yee[1]

[1]Jet Propulsion Laboratory, California Institute of Technology, 4800 Oak Grove Drive, Pasadena, California 91109, USA

[2]Department of Marine Sciences, University of Connecticut Avery Point, Groton, Connecticut 06340, USA

[3]Analytical Imaging and Geophysics LLC, 4450 Arapahoe Ave., Boulder, Colorado 80303, USA

[4]Naval Research Laboratory, 4555 Overlook Avenue, S.W., Washington, DC 20375, USA

[5]Desert Research Institute, 2215 Raggio Parkway, Reno, Nevada 89512, USA

*Corresponding author: pantazis.mouroulis@jpl.nasa.gov

The design, characteristics, and first test flight results are described of the Portable Remote Imaging Spectrometer, an airborne sensor specifically designed to address the challenges of coastal ocean remote sensing. The sensor incorporates several technologies that are demonstrated for the first time, to the best of our knowledge, in a working system in order to achieve a high performance level in terms of uniformity, signal-to-noise ratio, low polarization sensitivity, low stray light, and high spatial resolution. The instrument covers the 350–1050 nm spectral range with a 2.83 nm sampling per pixel, and a 0.88 mrad instantaneous field of view, with 608 cross-track pixels in a pushbroom configuration. Two additional infrared channels (1240 and 1610 nm) are measured by a spot radiometer housed in the same head. The spectrometer design is based on an optically fast (F/1.8) Dyson design form coupled to a wide angle two-mirror telescope in a configuration that minimizes polarization sensitivity without the use of a depolarizer. A grating with minimum polarization sensitivity and broadband efficiency was fabricated as well as a slit assembly with black (etched) silicon surface to minimize backscatter. First flight results over calibration sites as well as Monterey Bay in California have demonstrated good agreement between *in situ* and remotely sensed data, confirming the potential value of the sensor to the coastal ocean science community. © 2014 Optical Society of America

OCIS codes: (110.4234) Multispectral and hyperspectral imaging; (120.0280) Remote sensing and sensors; (280.4788) Optical sensing and sensors; (280.4991) Passive remote sensing; (120.6200) Spectrometers and spectroscopic instrumentation; (010.4450) Oceanic optics.
http://dx.doi.org/10.1364/AO.53.001363

1. Introduction

The coastal zone is home to a high fraction of humanity and is increasingly affected by natural and human-induced events, such as tsunamis, storm

events, toxic tidal blooms, nutrient runoffs, or oil spills. The measurement and monitoring of the diverse constituents of coastal zones—including optically complex water with phytoplankton, sediments, and colored dissolved organic matter, benthic ecosystems (corals, submerged, floating, and emergent aquatic vegetation), and other coastal vegetation such as salt marshes—require contiguous spectroscopic or "hyperspectral" measurements and imagery collected at appropriate time and space scales. Coastal floating, emergent, and benthic vegetation is often patchy and requires high-spatial-resolution imagery, but is fairly stable over seasonal time frames and requires less temporal resolution. On the other hand, plumes and blooms of phytoplankton and sediment can vary on time scales of hours to days.

Imaging spectroscopy in the visible and near-infrared (VNIR) spectral region is acknowledged as an important technique for monitoring and understanding coastal ocean processes. It has been successfully used, for example, to map seagrass leaf area index or monitor algal blooms and coral health [1–3].

Current satellite data provide a broad overview of these events but do not have the necessary spectral, spatial, and temporal resolution to sufficiently characterize these ecosystems and episodic events. MODIS [4] and the more recent VIIRS [5] have spatial resolution in the 250–1000 m range and do not provide spectrally contiguous data. MERIS [6] has similar spatial-resolution limitations although it provided contiguous spectral data that were aggregated into broader bands. HICO [7] on board the International Space Station (ISS) provides contiguous spectra, and, at ~100 m, higher spatial resolution, but still not optimum for the varied coastal environment. HICO coverage is also limited by the ISS orbit.

Airborne sensors fill an important niche in coastal zone observations by providing optimally timed and located high spectral and temporal resolution data that are unavailable from satellites. Spatial resolution can reach 1 m or less with appropriate design, and can be used for fine scale study of coastal ecosystems and estuaries. The PHILLS sensor [8] and its essentially similar successor SAMSON [9] represented a first attempt to cover this observational gap.

An imaging spectrometer for the deep or coastal ocean must be optimized primarily for the VNIR region, as that region provides access to the available and relevant water constituent signatures. Focus on the VNIR spectral range provides the opportunity for performance advances over other general purpose or land-oriented sensors that must cover the solar-reflected spectrum up to the strong water vapor atmospheric absorption edge at ~2500 nm, such as AVIRIS [10], MaRS [11], or APEX [12]. A driving design factor for a coastal ocean instrument is the low signal returned from water targets, so light collection capacity and overall instrument efficiency must

be optimized for a target reflectance as little as 1%. At the same time, exposed sand can be very bright, so the instrument requires a broad dynamic range. In addition, and especially at the shorter wavelengths, the signal from the surface is overwhelmed by atmospheric scatter, which is polarization-sensitive and wavelength-dependent. Also, spatial variation in coastal areas can be of a fine scale, below 1 m, necessitating high spatial resolution and a high degree of instrument response uniformity [13,14]. Thus an instrument optimized for the coastal ocean must provide high throughput and dynamic range, as well as minimum polarization sensitivity [15,16] and high response uniformity. Radiometric accuracy as well as minimization of stray light and detector readout smear are additional critical considerations [7,17–19]. In this paper we report on a system that was designed to address all these considerations with maximum performance in each case.

The optical design of the Portable Remote Imaging Spectrometer (PRISM) was conceived in 2008 [20], and development of the full sensor started in 2009. The sensor had engineering and science test flights in the spring and summer of 2012. It has now become available to the science community as a NASA facility instrument.

2. Sensor Overview

PRISM comprises a pushbroom imaging spectrometer covering the near-UV to near-IR range (350–1050 nm) and a separate spot radiometer covering two short-wave infrared (SWIR) bands at 1240 and 1610 nm, respectively. An instrument schematic is shown in Fig. 1.

The complete sensor comprises the optical head assembly (OHA) and control electronics. The OHA comprises a vacuum vessel with the spectrometer and SWIR radiometer inside, an aircraft interface/mounting plate, an INS/GPS unit attached to the optical head for enabling precise orthorectification and geolocation, as well as a preamplifier and A–D converter for the detector electronics. The vacuum vessel
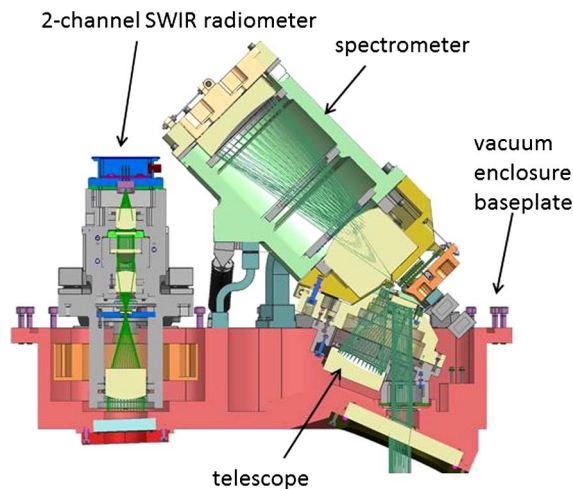

Fig. 1. PRISM instrument optical head assembly layout.

shell is temperature-stabilized to around 26°C with external strip heaters. The required vacuum level for stable operation is <0.4 Pa (3 mTorr). The instrument retains this vacuum level through a typical flight without on-board pumping. Three commercial vibration isolators prevent high frequency vibration from transmitting to the optics and detectors. The OHA unit, including the mounting plate, weighs approximately 40 kg and has approximate dimensions of 55 cm × 50 cm × 40 cm.

The control computer passes the high-speed data stream to a CORE DVR data-recording unit where the data are stored on solid-state drives with a total capacity of 1.5 TB (expandable). The drives are removed after the flight, and the data are downloaded to another computer for same-day processing. The remaining electronics are dedicated to thermal control and data logging. The temperature of the instruments inside the vacuum vessel is kept at 25°C through bidirectional thermoelectric coolers. The spectrometer detector is running at a temperature of about 7°C. There are also two shutters, one for the SWIR radiometer and one for the spectrometer to provide dark frame acquisition. The operator's task is to click on a software "record" or "stop" button at the beginning and end of a flight line. Dark frames are acquired automatically at those times. If desired, the computer displays temperature data from the various sensor locations in the OHA, in addition to a "waterfall" display of the data being acquired. Data are digitized to 14 bits. Geolocation data are acquired from a Systron–Donner C-MIGITS III unit and correlated to the focal plane array (FPA) readout within ± 100 μs to ensure position and pointing knowledge within one instantaneous field of view (IFOV). The position and pointing information are used with the PRISM optical camera model and surface elevation information to generate orthorectified measurement products. An uninterruptible power supply (UPS) provides power between hangar and aircraft power during take-off and landing.

In deployment, PRISM is accompanied by a calibration monitoring assembly comprising a 12″ diameter Labsphere integrating sphere with a customized port, stabilized tungsten halogen source, calibrated broadband detector, and low-pressure Hg lamp source. During calibration, the integrating sphere is hermetically mated to the spectrometer and SWIR radiometer windows in succession using a simple clip-on mechanism. A reading of the sphere output is taken by the instrument before and after the flight without removing it from the aircraft mount. This characterization step serves as an additional insurance against drifts, but may be omitted in the future once the long-term stability characteristics of the sensor have been established.

3. Optical Specifications

The spectrometer optical specifications are summarized in Table 1. These values represent measured data. Details of the measurements are given in

Table 1. Spectrometer Characteristics

Spectral	Range	349.9–1053.5 nm
	Sampling	2.83 nm
	Resolution (FWHM)	3.5 nm typ
	Calibration uncertainty	<0.1 nm
Spatial	Field of view (FOV)	30.7°
	IFOV sampling	0.882 mrad
	IFOV resolution (FWHM)	0.97 mrad
	Cross-track spatial pixels	608
Radiometric	Range	0%–99% R
	Sampling	14 bit
	Calibration uncertainty	<2%
	Signal-to-noise ratio[a]	500 at 450 nm
	Polarization variation	<1%
Uniformity	Spectral cross-track uniformity	>95%
	Spectral IFOV uniformity	>95%

[a]At a single integration (167 Hz rate) and three-band aggregate (8.5 nm), 5% reflectance, 45° solar zenith, MODTRAN standard atmosphere.

Section 5. The terminology of Table 1 should be self-evident with the potential exception of the last two rows. Spectral cross-track uniformity characterizes the variation of the spectral calibration with respect to the cross-track spatial sample of the pushbroom instrument. It includes what has been called "smile" (curvature of the monochromatic slit image), clocking misalignment (net rotation between slit image and FPA), and through-field variation of the spectral response function (SRF) FWHM. The spectral IFOV uniformity characterizes the spectral variation of the spatial response, and includes what is often called "keystone" (chromatic variation of magnification), the net rotational misalignment between grating grooves and FPA, and the chromatic variation of the cross-track spatial response function shape. These values have been reduced to fractional pixel errors as explained in Section 5. A value of 100% indicates no error, while a value of 99% would indicate a total error equivalent to a smile or keystone of 1% of a pixel (0.27 μm) across the field or wavelength band.

The characteristics of the SWIR radiometer are given in Table 2. These, too, represent measured values, with the measurement details given in Section 5. The two bands have been chosen on the basis that the corresponding atmospheric windows provide minimum sensitivity to small spectral shifts. While the dynamic range of the spectrometer covers maximum to minimum reflectivity, the SWIR radiometer is

Table 2. SWIR Radiometer Characteristics

Parameter	Channel 1	Channel 2
Channel center (nm)	1242	1608
Bandwidth (nm, FWHM)	22	56
FOV (mrad, FWHM)	2.4	2.4
Boresight knowledge (mrad, relative to spectrometer)	0.05	0.05
Sampling	13 bit	13 bit
SNR at 1.2 mW/cm² sr	325	390

Table 3.   Performance Enabling Technologies and Techniques

Performance Metric	System Parameter	Enabling Technology
SNR	Throughput ($F = 1.8$), transmittance	Dyson spectrometer, two-mirror telescope design.
Dynamic range	Rapid readout rate (167 Hz)	Teledyne HyViSI detector, custom readout electronics
Polarization insensitivity	Angles of incidence, grating response	Optical design, grating groove design, coatings
Uniformity	Optical prescription	Dyson design, concave grating, lithographic slit
Stray light suppression	Optical surfaces, slit, grating	Optical design, coating and filter design, black Si slit, low scatter grating
Calibration stability	Operating temperature ($\sim$25°C), vibration response	Optomechanical design, detector mount, athermalization
No image smear	Snapshot readout	Teledyne HyViSI detector

used only over water. The theoretical basis is that the signal received in those channels over clear and deep water is primarily due to light scattered by atmospheric aerosols and can therefore be used to constrain atmospheric correction parameters. However, if there is significant surface reflectance at those wavelengths, the aerosol signal cannot be decoupled from the unknown surface signal, making the SWIR channels unusable [21].

4. Instrument Design

In order to achieve the required performance, the PRISM spectrometer utilizes an array of new or novel technologies and design techniques. These are summarized in Table 3 and explained in the following sections. To the best of our knowledge, most of these techniques are implemented for the first time, whether in isolation or in combination, in PRISM.

A. Optical System

The basic spectrometer optical design was proposed in [20], and modifications to it that improved manufacturability and reduced stray light were discussed in [22]. We include here a brief narrative for completeness. The spectrometer is of the Dyson design form [23], which permits a high throughput (F/1.8 in this case) and also provides low angles of incidence for controlling polarization variation. In order to provide adequate clearance between slit and detector without affecting polarization, a folding prism is employed that operates in total internal reflection (TIR). The prism and an additional flat plate are bonded to a thick planoconvex element (Fig. 2) using cement with high transmittance at 350 nm and throughout the band. All transmissive elements
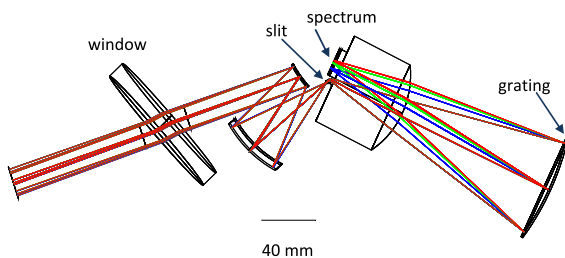

Fig. 2. Ray trace of the telescope/spectrometer system in the direction of dispersion. The grating is the concave rightmost element.

are made of fused silica. An antireflection (A/R) coated vacuum window is added to the design at an angle that, in conjunction with the telescope mirror coatings, minimizes the overall instrument polarization sensitivity.

The two (oblate ellipsoidal) telescope mirrors were fabricated on BK7 glass substrates by Optimax and coated with bare Al at JPL, the coating chosen on the basis of polarization analysis. The TIR prism, lens, and flat plate assembly were fabricated, bonded, and coated with a broadband A/R coating by JML Optics. The coating reflectance was measured at <1.1% throughout the wavelength range 350–1050 nm.

Both the telescope and the spectrometer were assembled and aligned with simple contact and bond techniques, using precisely machined spacer tubes and/or contact edges. The telescope achieved a p-v mean wavefront error of 1.1λ at 633 nm across the field, consistent with the design expectation. For the spectrometer, a geometric image location test was performed that confirmed the accuracy of the assembly, and also a semi-quantitative star test across the field to confirm that the point spread functions had the expected aberration content. In place of subsystem test results, we will present in the next section the full system response.

1. Diffraction Grating

The concave diffraction grating was fabricated using electron-beam-lithography techniques [24]. The grating diameter is 67.8 mm. The glass substrate was fabricated by Applied Optics, Inc., using glass with a high thermal expansion coefficient (S-PHM52), since analysis indicated this to be preferred for overall system athermalization. The grating is coated with a bare Al coating. A photograph is shown in Fig. 3 along with an atomic force microscope scan of the groove shape. This shape has been optimized for broadband response throughout the spectrometer range as well as low polarization sensitivity. The groove pitch is approximately 14 μm

The efficiency of the grating as well as its polarization sensitivity are shown in Fig. 4. These curves are derived from the measured grating profile of Fig. 3, which is input into PCGrate grating efficiency computation software. This process has provided good agreement with direct efficiency
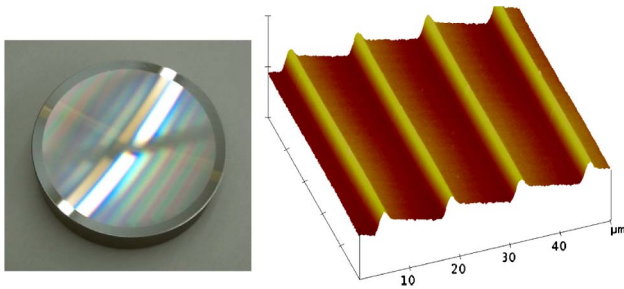
Fig. 3. Photograph of the concave diffraction grating and measured groove profile of the same. The blazed first-order can be seen displaced from the zero-order observed most strongly on the unexposed outside ring.

measurements. Polarization sensitivity is defined as $(I_p - I_s)/(I_p + I_s)$.

2. Slit Assembly

The slit assembly is a critical element of the overall design. First, the straightness and width uniformity of the slit must support the stringent uniformity specifications of the spectrometer. This is accomplished with a lithographic technique that creates the slit on a silicon nitride membrane supported on a Si wafer. The resulting slit is straight and uniform to within 100 nm or better (slit dimensions 16.47 mm × 0.027 mm). In addition, the slit assembly must be used to control stray light. Light reflected from the detector or order-sorting filter (OSF) is returned toward the slit at high efficiency and can then be redirected toward the spectrometer creating stray light. This can be handled by tilting the slit plane so that reflections from it end up outside the spectrometer collecting aperture. However, the tight clearances of the Dyson design do not allow significant tilting, the slit being located <1 mm before the TIR prism entrance face. To resolve this problem, we used an etching technique that creates an absorbing structure on the surface (black Si). The surface texturing is accomplished via a silicon cryo-etch process, which enables the black surface
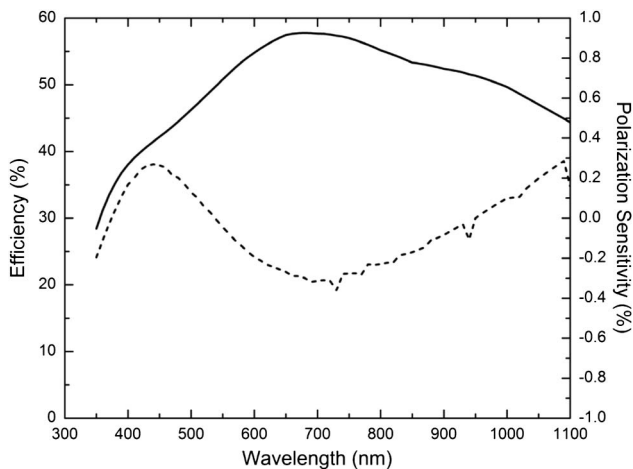

Fig. 4. Overall efficiency (solid line) and variation of efficiency with polarization (dashed line) for the PRISM diffraction grating.

to be precisely defined right up to the edge of the slit. The integrated diffuse reflectance of the black-Si surface has been measured to be below 1% throughout the visible and SWIR wavelength range. In addition, this silicon black is completely inorganic, does not outgas, and does not suffer from adhesion problems that may be encountered with surface deposition techniques (e.g., carbon nanotubes, black paint). The other side of the wafer (facing the telescope) is coated with gold. In order to reduce the likelihood of ghost reflections on the telescope side, we also incorporated a black-Si baffle that blocks most of the backreflection on the telescope side, too. Thus practically all the light from the telescope either is baffled before the slit assembly or is incident on the black-Si baffle if it does not pass through the slit.

3. Order-Sorting Filter

Since the PRISM spectrometer covers more than an octave, an OSF is needed. While there has been at least one similar instrument that did not utilize one [7], it should be clear that radiometric accuracy is compromised to some extent in the presence of order overlap even if correction algorithms are employed. A two-band filter is used in PRISM. The filter is deposited on a 1 mm thick fused silica substrate that is placed in near contact with the photodetector surface (~0.1 mm away). One side of the substrate has the OSF coating, while the other side (away from the detector) is coated with a broadband A/R coating, the reflectance of which was measured to be ~1% throughout the band with a maximum value of 1.5% around 400 nm. The order-sorting function is achieved with a long-pass segment that blocks wavelengths below 600 nm. The wavelength band below this wavelength does not strictly require any filter, but a bandpass segment was added to help reduce stray light. Thus the overall filter comprises a bandpass and a long-pass segment, joined by a "seam" that is physically located at a wavelength of ~610 nm. The seam is 2–3 pixels wide, and detector pixels immediately below it have a compromised radiometric response. The seam location was chosen to have minimum impact on the scientific return of the instrument. The corresponding spectral bands can either be removed altogether from the data or be used with appropriate caution. The filter segments are slightly oversized and surrounded by a black coating of low reflectivity ~5%. The zero-order beam is incident on this coating.

The total filter transmittance is shown in Fig. 5. An unfortunate and unintended fall-off is seen below 380 nm, which had to be accepted due to cost and schedule considerations. The filter seam transition wavelengths are also indicated by the dip at around 620 nm. The transition wavelengths are evident in this graph not because of the filter seam itself but rather because the cut-on wavelength of the long-pass segment was slightly longer than anticipated. Ideally the high transmittance regions of the two
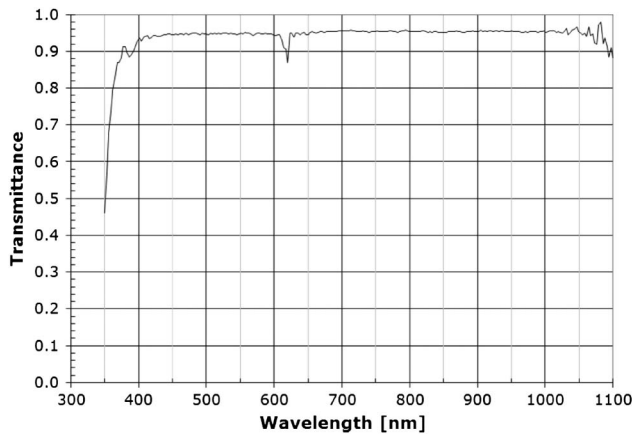
Fig. 5. OSF transmittance through wavelength. The graph is a composite of a bandpass filter transmittance at the short wavelengths (below 620 nm) and a long-pass filter above that range.

segments would overlap fully and the transmittance dip would not be seen.

B. Optomechanical Design

The spectrometer optomechanical design was required to meet stringent stability specifications in addition to solving the tight clearance problems inherent in a Dyson spectrometer with concentric spherical surfaces. The design succeeded in every respect. Full details are outside the scope of this paper, but we give below a summary of the features that are critical for understanding spectrometer performance.

The spectrometer body is made of 6061 aluminum alloy, while the grating and detector mounts are made of 7075 alloy for additional stiffness. The fused silica Dyson lens is bonded on titanium pads that connect to the aluminum body, to ease the large thermal expansion coefficient mismatch between aluminum and fused silica. Although in operation the spectrometer body remains at near room temperature, this precaution ensures sensor survival over the temperature range from −20 to 60°C or more.

The two spectrometer optical elements, grating and Dyson lens assembly, are aligned using a simple contact technique with a precisely machined tube. After alignment and bonding, the grating mount is removed from the spectrometer body in order to remove the alignment tube and insert a baffle tube. The grating mount is then returned kinematically to its previous position. The baffle tube contains two baffles, one approximately halfway between lens and grating, and another in close proximity to the lens curved surface that traces the beam footprint (Fig. 1). A locking adjustment rod is provided to permit rotation of the grating about its axis in order to achieve parallelism between the grooves and the slit. This final adjustment does not affect the previously achieved element alignment.

The FPA assembly makes use of a full six degrees of freedom kinematic adjustment mount with lockable adjusting rods. Three rods in the focus direction control focus, and spectral and spatial tilt. Two rods in the spectral direction control spectral location and clocking, while a single rod in the spatial direction controls position along the slit length.

The telescope assembly is semi-kinematically mated to the spectrometer body with a three-point interface and is secured to it using spherical washers that mate to conical seats. Focus shims can be inserted behind the washers. After completing alignment, shear bonds are used to secure all subassemblies.

Sag and modal analysis was performed on all assemblies. The requirement for first mode >240 Hz was exceeded by factors of 4–10 for subassemblies, and the first mode for the entire spectrometer/telescope assembly was computed at 684 Hz. Static 1g loading in every direction produced a negligible 0.012 mrad boresight error, and 1% of pixel (0.028 nm) spectral error. This performance assures instrument stability in an aircraft vibration environment.

C. Thermal Design

PRISM was originally conceived as a room-temperature, fully isothermal system. However, after delivery and testing of the FPA it was found that substantially improved operation resulted from a lower temperature. As a result, the FPA operates at around 7°C, near the limit of what can be achieved with the present thermal design. The rest of the spectrometer and SWIR radiometer operate at 22°C. All temperatures are controlled using thermoelectric (TEC) Peltier bidirectional elements that reject heat to the bottom plate of the vacuum shell through specially fabricated flexible thermal straps. The strap attaching to the FPA mount must satisfy especially stringent requirements in order not to impart stress or motion affecting spectral calibration while rejecting a substantial amount of heat. This is accomplished with an innovative two-arm strap [25]. The spectrometer and SWIR radiometer are attached to the bottom plate through insulating G-10 tubes. The minimum required vacuum level of 0.4 Pa is set by the onset of TEC performance degradation and subsequent reduction in stability. Film heaters are attached to the outside of the vacuum shell to maintain its temperature at around 26°C. This helps maintain thermal stability especially during high altitude flight in unpressurized platforms. Despite the massive glass elements, thermal equilibrium is reached relatively quickly. Thermal modeling indicates a ~2.5 h settling time from an initial start of 15 K below operating temperature. A simple thermal soak analysis shows a spectral calibration change of just more than 1% of a pixel for a 2 K spectrometer temperature change. The thermal design keeps the spectrometer temperature constant to within less than 1 K. The TECs are controlled by eight ThorLabs TED8020 controller modules.

Thermal data from thermistor sensors throughout the instrument record the temperature of the FPA,

spectrometer body, SWIR detectors, and SWIR body. All the data are recorded through an Agilent data logger and can be correlated with the FPA data stream, although there is normally no need to do so.

D. Focal Plane Array and Electronics

PRISM utilizes the Teledyne HyVISI 6604A silicon detector array, which is a 640×480 format with 27 μm square pixels. The detector array coating is chosen to maximize quantum efficiency throughout the spectrometer wavelength band [26]. Data provided by the manufacturer are shown in Fig. 6. We also performed a reflectivity measurement. The value 1-R shows close agreement with the manufacturer-provided data except near the material bandgap.

The main advantage of this array is the snapshot readout mode, which eliminates image smear caused by charge transfer in CCD devices. In addition, the relatively large pixel size and corresponding full well capacity of about 800 ke$^-$ permit a large throughput and reduce saturation concerns. The slit image occupies 608 fully illuminated pixels, the slit itself being 610 pixels long. There are altogether 248 spectral bands, and those are read out at a faster rate than would be required for all 480 rows. This rate is 167 Hz, corresponding to a clock rate of 4.312 MHz. This fast readout rate also guards against saturation with bright targets such as sand. The rapid readout is made possible by separating the array in four quadrants (160×480) that are read simultaneously.

It was found that the edge pixels (a band of about 30 pixels all around the array perimeter) exhibit high dark current at room temperature (near saturation). The effect, however, diminishes rapidly with decreasing temperature. This issue forced operation of the detector at the lowest temperature that could be
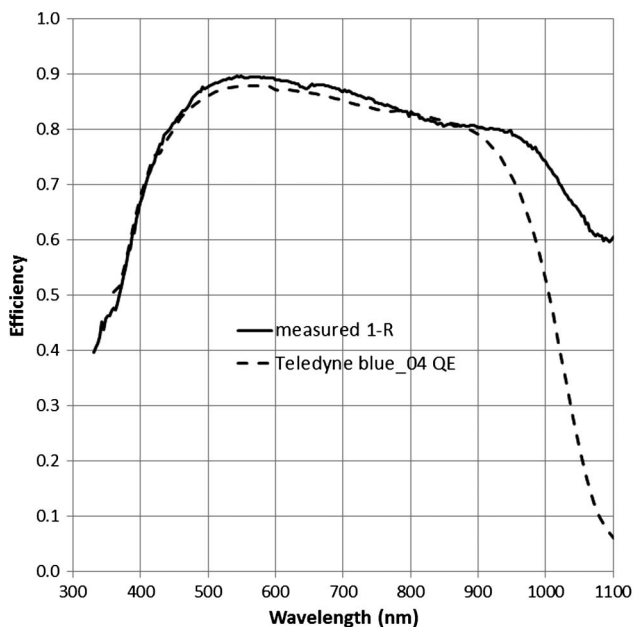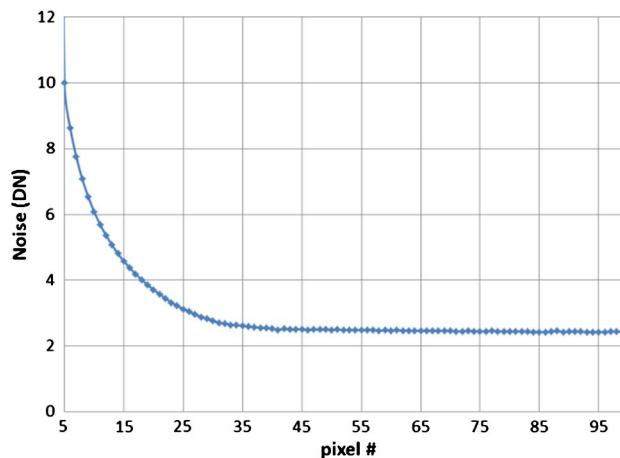

Fig. 7. Noise level as a function of pixel number (distance from the beginning of the array). The noise floor is due to the complete readout chain. The rise on the left is due to increased dark current in those pixels. Wavelength increases to the right. The first reported spectral channel is #19 (349.9 nm).

achieved with the original thermal system configuration (~ 7°C). An even lower temperature would have been desirable and may be implemented in future upgrades. The noise affects the short wavelength channels that are closest to the edge of the array. Figure 7 shows the effect of the increased dark current on the noise behavior of the first 100 spectral channels. In the spatial direction, the edge dark current effect unfortunately defeated the purpose of using a shorter slit than the array in order to monitor the dark signal level through the unilluminated pixels. It can be seen that the noise at the first reported spectral channel (pixel #19, 349.9 nm) is ~ 3.9 DN rms of the 16384 DN range or a little less than twice the noise floor that is due to the rest of the system (2.5 DN rms under the test conditions). Unlike the rise to the left, the noise floor is not temperature-sensitive. The increased noise effect is negligible by pixel #35 (395.2 nm).

E. SWIR Radiometer Design

The SWIR radiometer is intended to assist with atmospheric correction. The optical design comprises a simple telescope objective, a pinhole (field stop), identical recollimating and focusing lenses, a dichroic beamsplitter, and two bandpass filters. A schematic superposed on an optical system ray trace is shown in Fig. 8. The cemented doublets are made from thermally matched glasses and are A/R coated for both wavelength bands. The 1610 nm band center and 60 nm bandwidth have been chosen over the more commonly recommended 1640 nm/40 nm [27] on the basis of reduced sensitivity to small spectral shifts. Omitted from this figure is the vacuum window, which is used as a blocking filter to prevent radiation below 1150 nm from entering the system. The InGaAs photodiodes (Hamamatsu G8376) are 0.2 mm in diameter, which was chosen as a best balance between alignment tolerance/mechanical

Fig. 6. Quantum efficiency of PRISM HyvISI detector array as provided by the manufacturer compared with measurement of reflectivity.
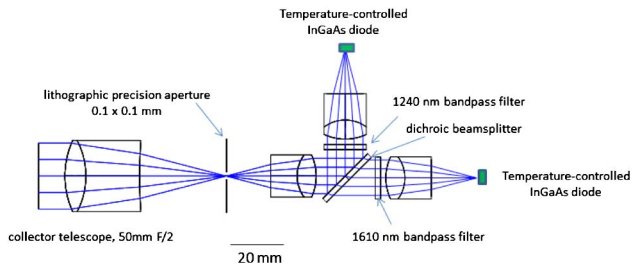
Fig. 8. Schematic of the SWIR radiometer arrangement. Not shown is the vacuum window and a Uniblitz NS15B shutter inserted after the pinhole that is used for collecting dark frames.

stability on the one hand, and noise on the other. The diode temperature is stabilized with integral TECs.

Due to the high sensitivity required of the electronic circuit, a fully differential amplifier configuration is employed that minimizes bias voltage and the associated dark current. After preamplification, the photodiode output is routed to the spectrometer A–D converter, combined with the spectrometer FPA, and read out as an additional spectral band, with the corresponding field pixels shared redundantly between the two detectors. The bidirectional output of the SWIR circuit combined with the positive-only input to the A–D converter leads to the loss of one bit of quantization.

5. Laboratory Tests and Calibration

For most laboratory tests, the instrument head was positioned on a goniometric stage that allowed rotation about the telescope entrance pupil, thus offering access to any field point. A luminous object (scanning slit or optical fiber) was placed at the focal point of an off-axis 750 mm parabolic collimator (OAP) with $\lambda/4$ surface quality, which sent the collimated beam into the spectrometer aperture through a set of adjustable fold mirrors. The instrument aperture (16.7 mm) samples only a small fraction of the much larger 4″ (100 mm) collimator aperture, thus ensuring a diffraction-limited beam even as the scanned slit moves away from the focal point, with the collimator operating at an effective F/45.

A. Spectral Characteristics

To obtain the SRF of the spectrometer, the scanning slit is replaced by a large (1.2 mm core diameter) optical fiber, which is fed by a wavelength-scanning double monochromator (Spectral Systems DK242). The fiber size ensures that the instrument slit is overfilled, accounting for the magnification factor between the collimator and the PRISM telescope. The fiber mode distribution was observed in the far field to ensure uniformity of illumination. The monochromator is then scanned in wavelength and the instrument response recorded. The procedure was repeated for five different field points. The monochromator output was calibrated using spectral lamps. At the slit width used, the monochromator output was found to be nearly Gaussian with a FWHM of <0.6 nm. This leads to an acceptably small
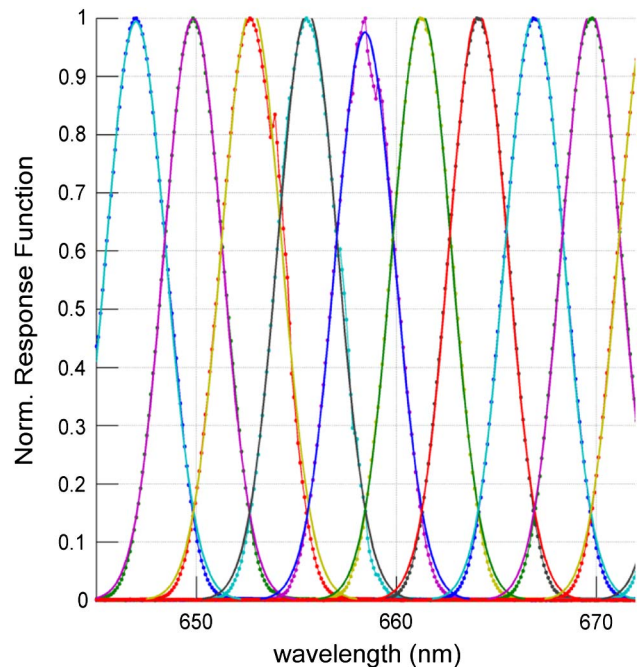

Fig. 9. Typical SRFs obtained with a scanning monochromator.

~2% overestimate of the actual PRISM SRF FWHM [28,29].

A set of representative SRFs is given in Fig. 9. Shown in the figure are the raw recorded data as well as a Gaussian fit function for every channel. It can be seen that the Gaussian approximation is very good, with a slight though systematic difference below ~0.1. The occasional irregular points, seen, for example, on the third and fifth peaks from the left, are due to occasional jitter in the scanning mechanism, which could have been reduced by a slower scan but would have then led to exceedingly long recording times. The irregularities were judged acceptable, especially as the overall purpose of these measurements was to determine the overall width and shape of the SRFs but not the centroid location.
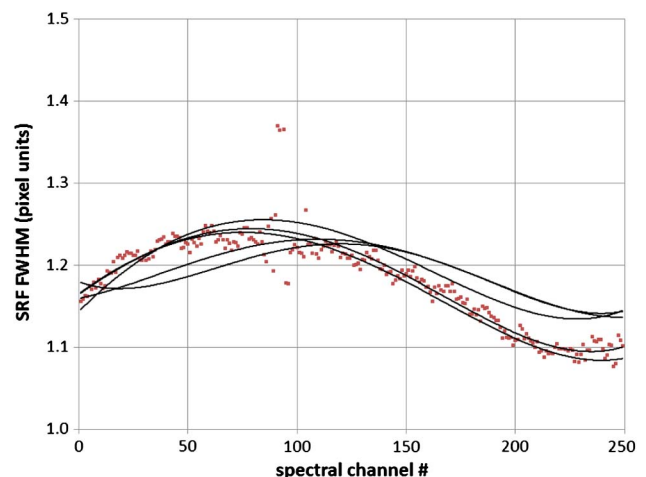

Fig. 10. SRF FWHM from Gaussian fit as a function of wavelength (spectral channel #) for five field points across the PRISM FOV. Five interpolated lines are shown and one set of raw points. The field points are ±14.4°, ±8°, and 0°.

Table 4. PRISM Calibration Wavelengths and FPA Centroid Locations

	Hg	Hg	Hg	Ne	Hg
λ (nm)	404.66	435.83	546.07	632.8	1013.98
Centroid	38.39	49.32	88.29	118.87	253.11

Figure 10 shows the SRF FWHM as a function of the spectral channel for five field points. Fourth-order fit polynomials are shown, together with the raw points of only one of the curves for clarity and to give an idea of the fit (R² = 0.95 excluding four points at the OSF seam). The effect of the OSF seam can be seen around channel 93 on the raw points. The noise in these curves arises from measurement artifacts such as those shown in Fig. 9. The through-field variation, as measured by the maximum vertical distance between the fourth-order curves, has a maximum of ~6% of pixel width at the long wavelength end.

For establishing the centroid location, we employ an integrating sphere fed by a He–Ne laser and a low-pressure Hg lamp with known wavelengths. The wavelength centers are shown in Table 4, together with the corresponding centroid locations in pixel units starting from pixel 1 (so the first reported spectral channel is 19). A linear approximation is possible, but design data lead us to expect a slight nonlinearity of about 0.5 nm over the entire band that is due to the catadioptric nature of the Dyson form. For precise atmospheric correction, a quadratic curve can be used: $y = 2.812\text{E} - 05x^2 + 2.82916x + 296.099$, where x is an integer between 19 and 268 and y is the corresponding center wavelength. There is good agreement between this curve and the one expected from design values.

This precise wavelength calibration is not useful unless it is maintained through the field. For this to happen, the spectrometer must display no smile (curvature of the monochromatic slit image) or rotation of the focal plane relative to the slit image. Figure 11 is a representation of these effects, and it can be seen that smile is very low, while spectral alignment is at around 2% of a pixel over the entire field, corresponding to a spectral accuracy of

0.057 nm. To arrive at a total spectral uniformity figure, we add this 2% error and also one half of the 6% FWHM variation [28], giving a total error of 5%, or spectral uniformity of 95% per Table 1.

B. Spatial Characteristics

The spatial characteristics of PRISM were established through measurement of the cross-track and along-track spatial response functions (CRF and ARF) through field and wavelength. These are measured by scanning a subpixel slit placed at the focal plane of a collimator illuminating the instrument aperture, and oriented parallel or perpendicular to the spectrometer slit. Representative ARFs are shown in Fig. 12, showing a small to negligible variation both through field and (more importantly) through wavelength. The FWHM of these functions is about 1.1 pixel units. A motion blur is effectively convolved with these functions in flight. The exact form of the motion blur function will depend on the

Fig. 12. (a) Normalized along-track response functions for several fields and one wavelength. The horizontal axis has been converted to pixel (slit) width units. (b) Normalized along-track response functions for one field and several wavelengths.
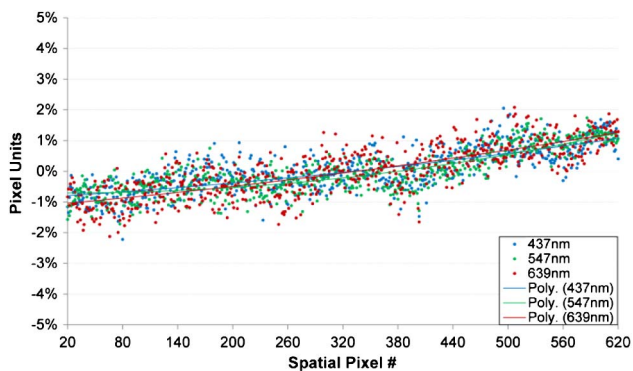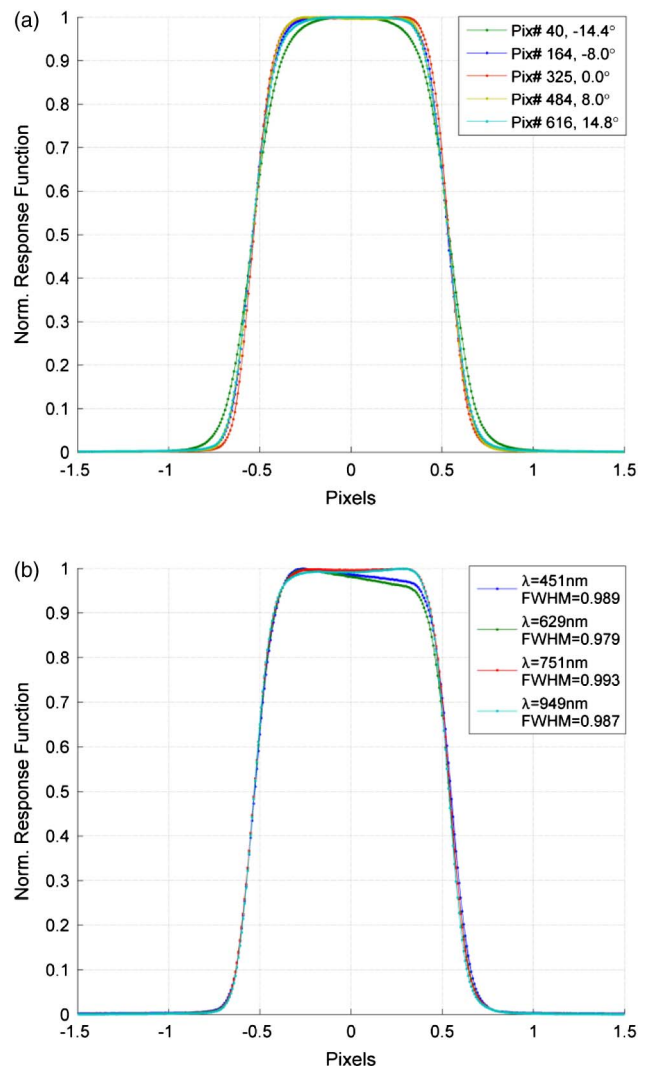
Fig. 11. Scatter plot of spectral channel centroids as a function of spatial location for three isolated wavelengths (Hg lamp 437 and 547 nm, and laser at 632.8 nm).
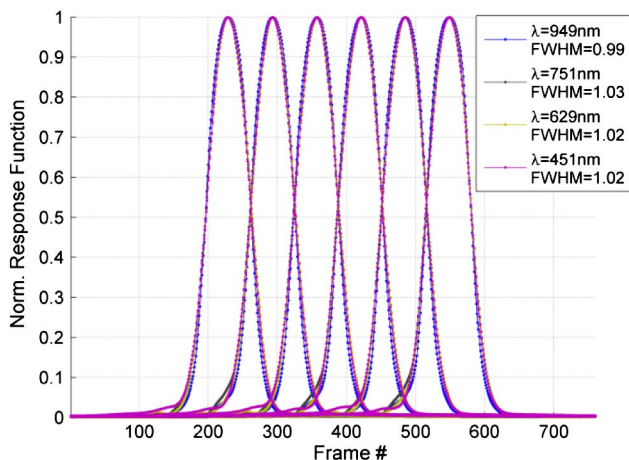
Fig. 13. Typical cross-track spatial response functions for adjacent pixels and several wavelengths.

altitude and speed of the aircraft. The short integration time of PRISM means that several frames may be averaged over a single IFOV; thus the image is normally oversampled in the forward direction (see also Section 6.A).

Representative CRFs are shown in Fig. 13 for adjacent pixels and wavelengths spanning the spectral range. The FWHM is again around 1.1 pixels. A small asymmetric tail is also visible in some functions. The origin of this effect is electronic rather than optical, as confirmed during detector testing, and can be diminished with further cooling of the detector, which may be implemented in a future upgrade. However, because these functions are not well described as Gaussians, we do not characterize the uniformity through the centroid and FWHM variation separately as was done in the previous section. Instead, we adopt a measure of the total chromatic variation of the CRF integral that extends to the adjacent pixels. This measure, similar to that proposed in [30], contains both center location and width variation and makes no assumptions about the shape of the curve. The total maximum integrated variation (nonuniformity) normalized to the CRF integral in the main pixel is <5%.

PRISM geometric calibration is shown in Fig. 14. The slit image projected at infinity is an arc with a curvature (sag) of about 0.8°. Measurement and theoretical analysis from the telescope design data agree closely.

C. Polarization Characteristics

The optical design of PRISM was driven by the requirement for low polarization sensitivity [21,22].
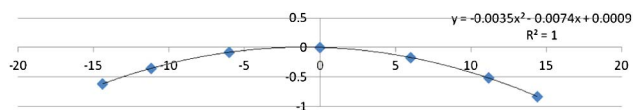

Fig. 14. Slit image projected to infinity is slightly curved. The measured data are shown here. For both axes, the units are degrees of angle.

To measure the polarization sensitivity of PRISM, a tungsten source was used to illuminate an integrating sphere that was placed at a distance of about 1 m from the spectrometer. A broadband Glan–Thompson linear polarizer of 2.5 cm aperture was placed in front of the spectrometer and rotated using a motorized stage, while the signal was recorded continuously. The polarizer aperture was comfortably larger than the spectrometer aperture of ~17 mm. A residual variation due to the test setup was present, as confirmed with a photodetector immediately behind the polarizer. (A wiregrid polarizer was also tried and found to provide inferior results.) The magnitude of this variation was <1% and had the same period as the rotation of the polarizer. This allowed us to remove it from the measurement, since the sensitivity of the system to a variable linear polarization is expressed as the magnitude of the second harmonic of the signal [27,31,32]. This magnitude was determined by a Fourier decomposition of the recorded signal as a function of angle (higher harmonics were in the noise). The result is plotted as a function of wavelength for five field points in Fig. 15. It can be seen that the variation remains everywhere at or below 1% with the exception of a spike occurring at the OSF seam. The user can choose whether or not to use the signal from these spectral channels with appropriate care. The lack of symmetry about the center of the field is not surprising in that such symmetry exists only at the telescope but not at the spectrometer, where the slit resides entirely on one side of the optical axis.

D. Radiometric Characteristics

It is first required to characterize the PRISM FPA for uniformity and noise. A gain uniformity assessment found only eight bad pixels over the entire usable area of the array based on the criterion that the pixel gain should be within 80% of the mean. For dark current assessment, Fig. 16 shows a dark signal map of the usable area of the array. The highest dark signal is around the perimeter of the array as already
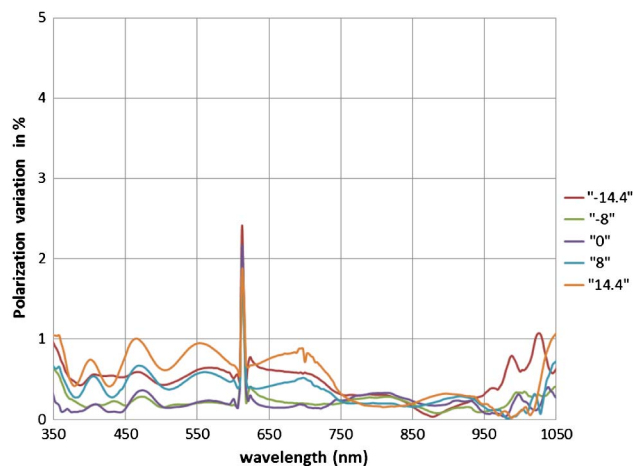

Fig. 15. Polarization variation throughout the spectral range for five positions spanning the FOV.
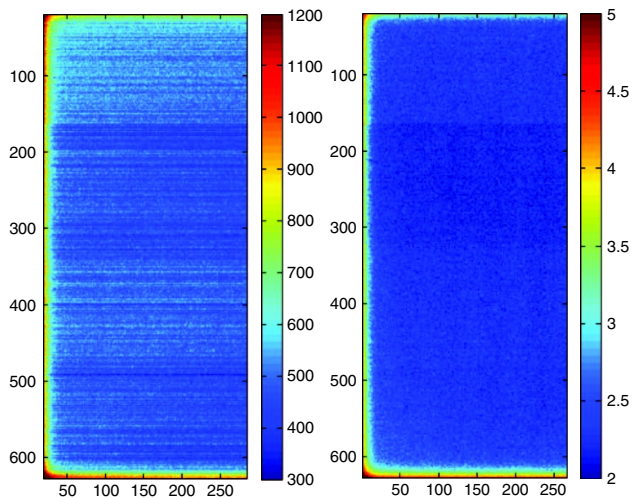
Fig. 16.   Left: dark signal average across the usable area of the detector array. Right: dark signal standard deviation. The color scale is in digital count (DN) in both cases.

explained. The weak horizontal striping is a readout effect, while there is also some mean level variation seen from top to bottom corresponding to the four detector quadrants. The standard deviation of the dark signal is also given in Fig. 16 and shows a slightly quieter second quadrant from the top. By far the most striking feature of these plots is the elevated values near the perimeter. Clearly, the corners of the array corresponding to the two ends of the field of view (FOV) and the short wavelength end have considerably worse performance than the rest; however, the total area affected is limited.

Flat field calibration for PRISM is obtained in two different ways. In the laboratory, a spectralon panel illuminated by a known source that covers ~1/3rd of the PRISM FOV is used while the spectrometer is scanned in the field direction. This ensures that all fields record the same irradiance. Figure 17 shows this result. The quadrant boundaries are more clearly visible in this case as horizontal stripes near rows 160, 320, and 480. A weak horizontal stripe seen near row 400 may be due to a small slit obstruction. The OSF seam is seen as a vertical stripe near column 110. The fringes seen on the long wavelength right end are due to an etalon effect in the detector material. Such fringing has been noticed before and is especially pronounced in thinned detectors [7]. The PRISM detector is not thinned, which accounts for the lack of fringing at the short wavelength end; however, the material transparency increases at the long wavelength end.

It is important that this flat field calibration should not vary in time or with the environment. For this reason, PRISM carries an integrating sphere that is used as a stability monitor, with data taken before and after a flight at the hangar. The measurement, over three days of flights, taken before and after each flight as well as at the hangar, confirms that the flat field is stable within ±0.4%. Comparison between the sphere and panel results demonstrates
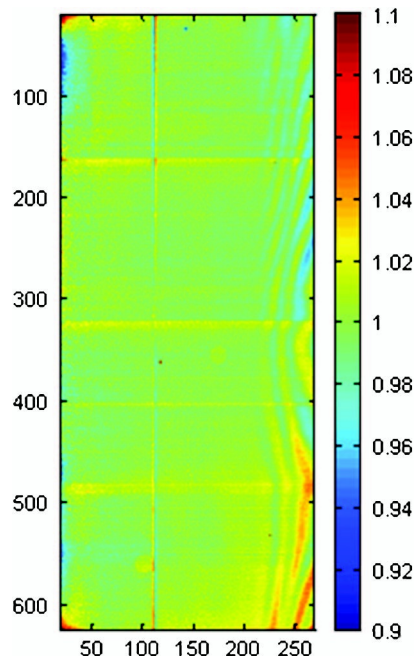

Fig. 17.   Flat field correction for PRISM. The figure results from illuminating PRISM with a spatially uniform radiance and removing the spectral variation by normalizing to the mean of all spatial channels for every wavelength.

that the sphere presents a small spatial variation that does not affect the stability assessment. The comparison may also be used to transfer the laboratory calibration to the sphere; however, we do not choose to do so due to the blue-poor sphere output that results in low signal over the short wavelength range.

A radiometric linearity test was also performed, using a calibrated tungsten source fed into an integrating sphere through a variable slit that controls the light level without affecting the source color temperature. Two independent monitoring detectors were also used. There are two levels of nonlinearity observed, as shown in Fig. 18. There is a (not unexpected) gross nonlinearity near the saturation level starting at around 85% of saturation. However,
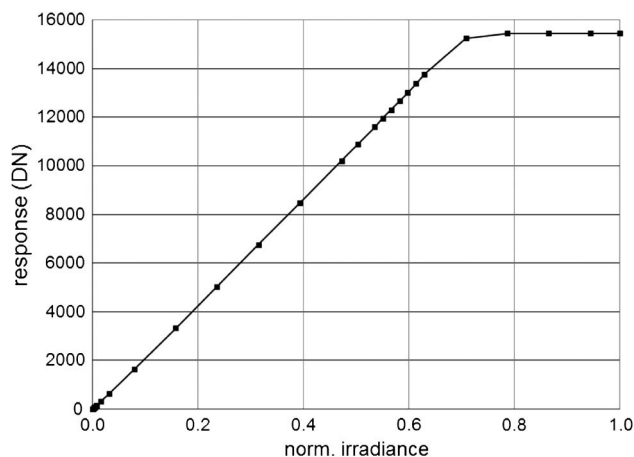

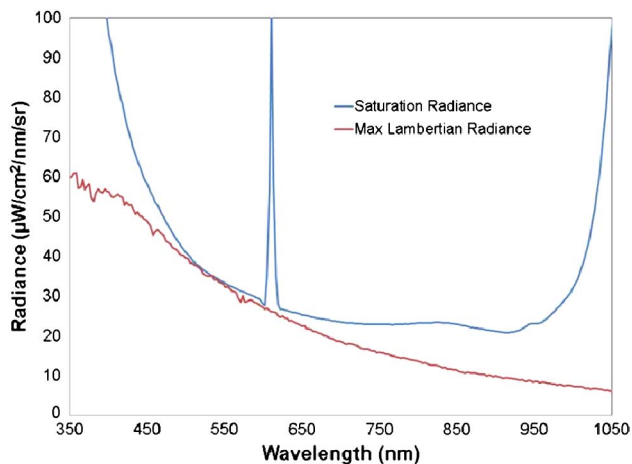Fig. 18.   Linearity of PRISM spectrometer signal chain.

Fig. 19. PRISM saturation radiance as a function of wavelength (top curve) compared with standard maximum target radiance.

Fig. 20. SNR through wavelength for low R (0.05) reference surface including standard atmosphere. Bottom curve is for a single 6 ms integration and one spectral channel (2.83 nm). Top curve aggregates three spectral channels (8.5 nm). PRISM SNR is normally higher due to forward oversampling.

PRISM generally avoids this region thanks to its short integration time (see also Fig. 19). A slight non-linearity is also observed, in the remainder of the range. The data up to about 13,000 DN are well fitted by a power curve of the type $y = ax^{1.015}$. This curve gives a peak error of < 0.1 DN up to 10 DN of signal, < 0.5 DN up to 60 DN, $< 1.7\%$ up to 600 DN, and $< 1\%$ to 13,000 DN. At the high radiance end, a quadratic curve can reduce the net error to below 0.1%. This fit exceeds the ocean sensor linearity requirements of [27]. Individual pixel values show some variation; the detailed data can be considered as needed.

The saturation characteristics of PRISM are shown in Fig. 19. Maximum Lambertian radiance is defined as the radiance from a unity reflectivity Lambertian surface illuminated by the sun directly overhead, and without intervening atmosphere. Barring specular reflections, this represents a safe upper limit for saturation. It can be seen that PRISM comes close to saturation at this level of radiance in the region near 500 nm. Thus PRISM has adequate headroom for practically every natural nonspecular target. The figure also shows that the instrument sensitivity is well balanced over the entire wavelength range, a result made possible by the e-beam structured groove grating.

The signal-to-noise ratio (SNR) characteristics of the spectrometer were assessed by first measuring signal and noise levels using a source of known radiance. This source was a NIST-traceable calibrated lamp placed at a distance of 0.5 m from a calibrated spectralon panel. The PRISM radiometric model accounts for the end-to-end throughput and noise properties including photon shot noise. The model was adjusted to the as-built instrument by matching it to the actual PRISM performance from the known source. The resulting correction was $< 10\%$ in the range of 480–950 nm, rising to ~30% toward the ends of the spectral range, most likely due to uncertainty in the theoretical detector QE at those ends. The as-built calibration model was then used to estimate
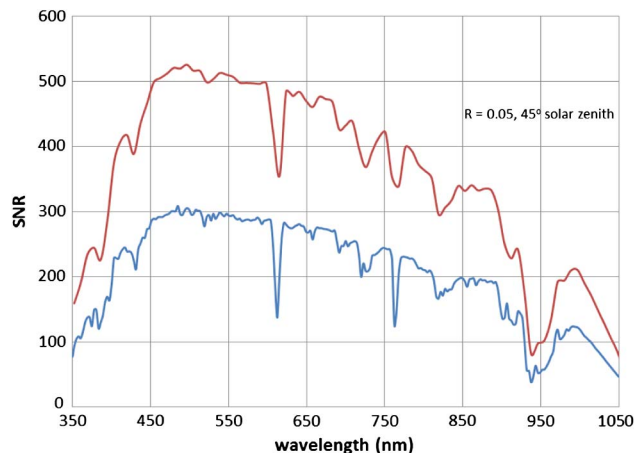
the SNR performance at the benchmark radiances using the standard MODTRAN [33,34] atmospheric model. The result is shown in Fig. 20 for one integration (6 ms) and a single spectral channel (2.83 nm) or a three-channel aggregate (8.5 nm) band. PRISM normally achieves higher SNR thanks to forward oversampling (in the along-track direction), depending on altitude and aircraft speed (see also Section 6).

Because PRISM was originally specified relative to AVIRIS [10] integration time and bandwidth, we note that summing frames to an equivalent AVIRIS rate of 12 fps and resampling to 10 nm bands results in a projected SNR of 2000 at 450 nm. A different and perhaps better way to quantify the comparison with AVIRIS is to consider what the spatial resolution (or equivalent frame rate) would be at which the two sensors have the same SNR. For an AVIRIS-equivalent SNR, PRISM achieves ~14x better spatial resolution, leading to the ability to resolve fine structure (<0.5 m) often required for applications such as aquatic vegetation mapping.

E. Stray Light and Related Effects

The PRISM design paid attention to the elimination of optical ghosts, and indeed such ghosts are not visible. Figure 21 shows the recorded PRISM output after illuminating the entire field with several laser lines. The distribution is smooth, and each line decays monotonically. Field variation is negligible, so we can present a field average section as representative. These characteristics enable the extension of spectral stray light correction algorithms [e.g., 35] developed for linear arrays to an area array spectrometer such as PRISM, although such correction has not been attempted to date.

The spatial stray light characteristics of PRISM can be assessed through an illuminated edge test. This experiment was performed by generating a sharp edge with black tape on an illuminated ground glass screen placed at the focal plane of a collimator
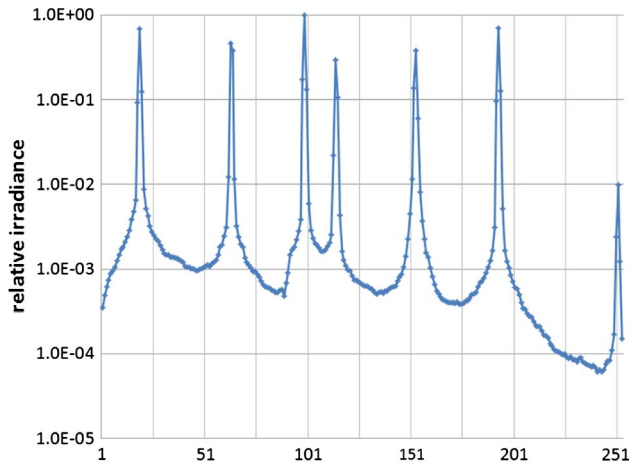
Fig. 21. Relative irradiance as a function of wavelength for several laser lines covering the entire field of view (FOV) and integrated along the spatial direction. Wavelength increases from left to right. The two extreme laser wavelengths are 405 and 1064 nm.

in front of the PRISM telescope. A tungsten halogen source was used, and the intensity was adjusted so the maximum signal for any wavelength was just below saturation. A test was performed to ensure that the radiance of the dark part of the mask was negligible. The along-track and cross-track characteristics are markedly different, as would be expected, since the along-track direction is not affected by the grating or spectrometer scatter. Figure 22 shows the results for a typical wavelength near the peak response. These results can be used in a deconvolution algorithm to reduce the effective stray light level over dark targets.

F. SWIR Radiometer Characteristics

As explained in Section 3, the SWIR radiometer is intended to aid with atmospheric correction. It has a FOV of approximately 2 mrad and is pointed toward the middle of the spectrometer FOV. The spatial alignment of the radiometer relative to the spectrometer was obtained by using a large aperture collimator and illuminating both instruments simultaneously. Scanning a slit produced simultaneous ARF and CRF data for the two instruments. This result has been shown in [36] and is not repeated here due to space limitations.

The spectral response of the two SWIR channels is shown in Fig. 23. This was measured with a scanning monochromator and a collimating lens in front of the instrument. The results have been summarized in Table 2. Signal-to-noise measurements were also performed for the SWIR radiometer using techniques similar to those of the spectrometer, with the results also shown in Table 2.

SWIR channel radiometric calibration was performed using the PRISM integrating sphere with its output referenced to the same NIST-traceable lamp and panel used for spectrometer calibration. A linearity test was also performed for the complete
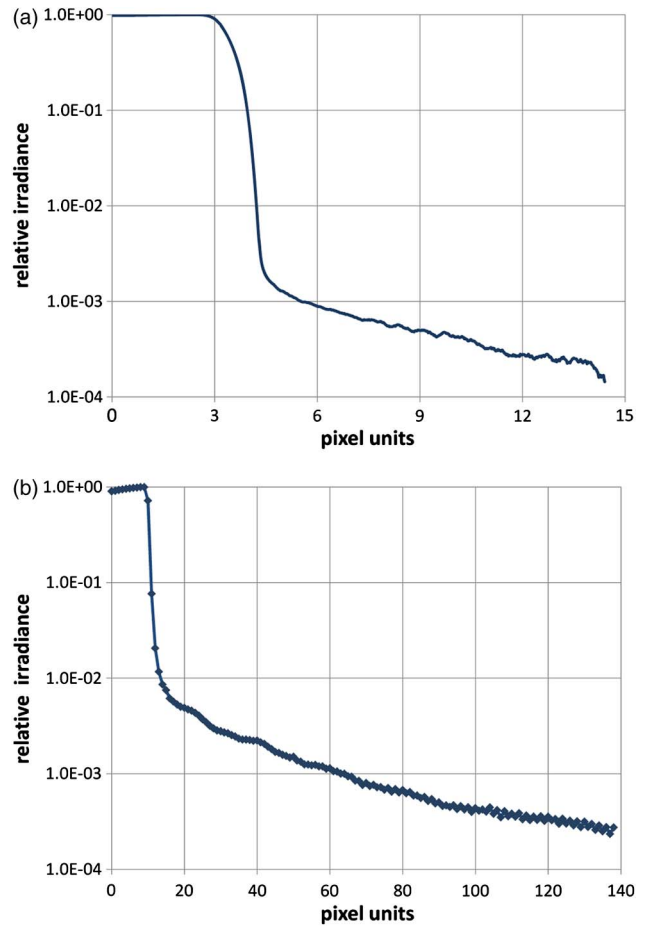

Fig. 22. (a) Along-track edge spread. (b) Cross-track edge spread. Point markers shown in (b) represent pixel values. In (a) individual points are not shown because they represent frames rather than pixels.

SWIR signal chain. The results are shown in Fig. 24. The test stopped when the saturation radiance was reached on one detector. The region of high radiance is not important because it implies that the bulk of the received signal comes from the surface rather than the atmosphere, thus invalidating the reason for implementing this instrument. The departure from linearity was significant especially at the low DN range. In order to obtain a satisfactory fit that keeps the errors below 0.5 DN at the low end and ~1% elsewhere, a three-piece quadratic fit was employed, separating low, mid-, and high radiance levels.

6. Field Tests

A brief overview of the flight results is presented here to confirm PRISM robustness in operation. The body of collected data is under processing for science product generation to be presented in future publications.

A. Results from the Engineering Flight

For its first test flight, PRISM was integrated on a Twin Otter aircraft operated by NASA Glenn Research Center. To assess in-flight spectral,
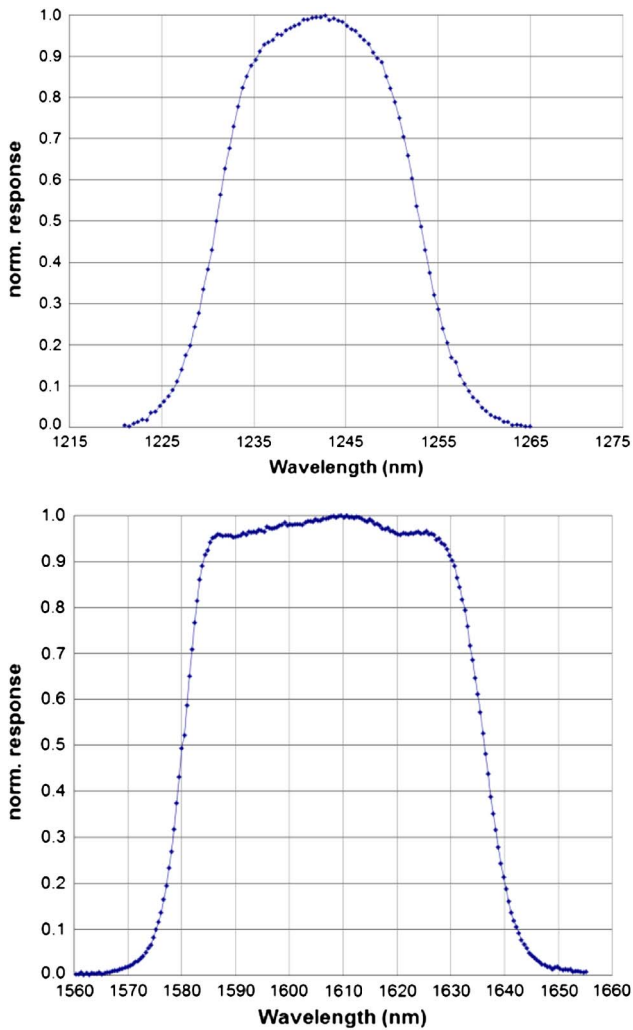
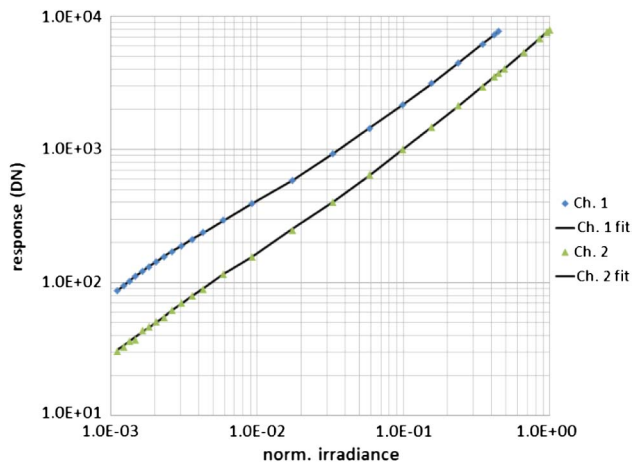Fig. 23.   Spectral response of the SWIR channels.

Fig. 24.   Radiometric calibration of SWIR channels, showing departure from linearity and piece-wise quadratic curve fit.
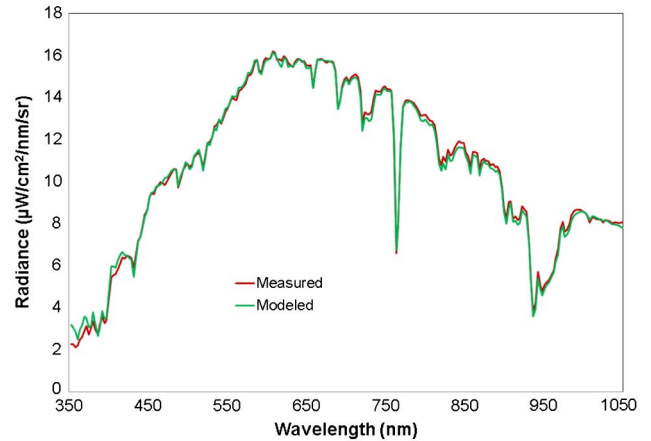

Fig. 25.   Top: demarcation target (blue tarp) and dry lakebed at Ivanpah Playa. Bottom: spectrum measured by PRISM compared with prediction from MODTRAN radiative transfer code.

radiometric, and spatial properties, a calibration validation experiment was held at Ivanpah Playa dry lake in California on 8 May 2012. Figure 25 shows the dry lakebed and a blue tarp demarcation target. The reflectance of the dry lakebed between two such tarps was measured with an ASD Inc. field spectrometer. Adjacent to the calibration site, atmosphere properties were measured with a 10-channel solar radiometer. The *in situ* measurements were used to constrain the MODTRAN [33,37] radiative transfer code and predict the radiance arriving at PRISM from the calibration target. A comparison of the predicted and PRISM measured radiance is also shown in Fig. 25. This comparison shows good in-flight radiometric calibration. The alignment of the solar and atmospheric absorption features (e.g., oxygen at 760 nm) confirms the laboratory spectral calibration of PRISM.

The fine spatial sampling capability of PRISM was assessed with an arrangement of 30 cm square ceramic tiles spread out on the dry lakebed surface. Figure 26 shows a raw PRISM image of the tiles. The separation between the tiles at the corner is 30 cm. This demonstrates the ability to spatially resolve objects at this scale.

To extend the engineering tests to dark water targets, another test flight was undertaken on 10 May 2012, over Lake Tahoe, a high altitude (1897 m) clear body of water that spans the California/Nevada border. From this flight we also demonstrated orthorectification from the integration inertial navigation system attached to the PRISM optical head and instrument camera model. Figure 27 shows a portion of an oversampled PRISM raw image, the corresponding orthorectified image of the Lake Tahoe shoreline,

Fig. 26. Raw PRISM image of 30 cm square tiles (seven tiles in the middle of the frame) placed on the dry lakebed surface, adjacent to the radiometric calibration target. The corner tile is separated by 30 cm from each of its neighbors.

as well as a set of extracted spectra. The spectra of dark water, bright beach, and terrestrial vegetation demonstrate the wide dynamic range of PRISM. The altitude and ground speed for this flight provided approximately seven samples per IFOV. Averaging the oversampled data in the along-track direction increases the SNR of the spectra for analysis. The success of the orthorectification algorithm can be judged by the straightness of the jetties and artificial boundaries.

The results from these engineering flights indicated good overall performance but also identified some needed hardware and software fixes that were implemented before the next field validation.

B. Preliminary Results from the Science Flight

The second field validation of PRISM occurred in the Monterey Bay region of California and focused on Elkhorn Slough, California, an estuary that provides a critical habitat for many threatened and endangered organisms including marine mammals, sharks, and seabirds. The PRISM sensor was integrated onto a Twin Otter aircraft (Twin Otter International). More than 400 GB of imagery was obtained including 12 flight lines over Elkhorn Slough and the adjacent Monterey Bay shelf at 1070 m (<1m/pixel), three lines at 3200 m height (∼3 m/pixel) extending 40 km into the bay and over the M1 research mooring maintained by the Monterey Bay Aquarium Research Institute (MBARI), and additional lines over Pinto Lake at 1070 m. The field campaign from 18 to 27 July 2012, led by the Coastal Ocean Laboratory for Optics and Remote Sensing (COLORS) laboratory at the University of Connecticut, involved collaboration between seven institutions including NASA JPL, NASA Ames, the Naval Research Lab, the University of California Santa Cruz, MBARI, and Moss Landing Marine Laboratories. Remote sensing reflectance *(Rrs)*, water-leaving radiance normalized to incident downwelling irradiance [38] was measured coincident with the PRISM overflights using a Field Spec portable spectrometer system (Analytical Spectral Devices) following the methods from [3].
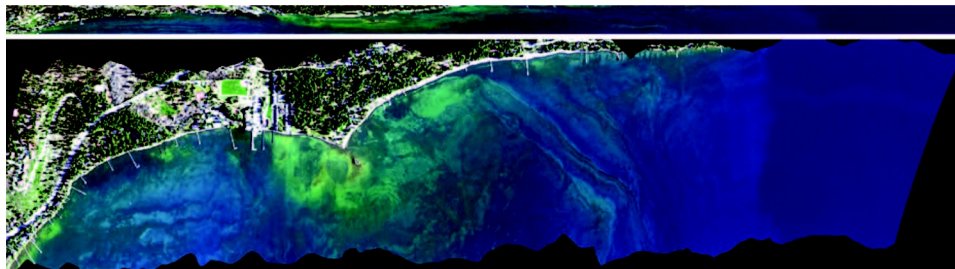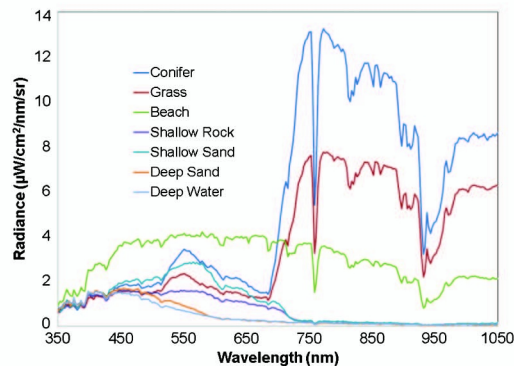
Fig. 27. (a) Top strip is the raw PRISM image showing along-track oversampling, which therefore appears stretched. This raw image is also available to the operator as a real-time "waterfall" display. The orthorectified image of the same area shows the Dollar Point coast of Lake Tahoe. (b) Spectra extracted from the PRISM Lake Tahoe data set testing the dynamic range of PRISM from dark water to rocky beach to terrestrial vegetation.
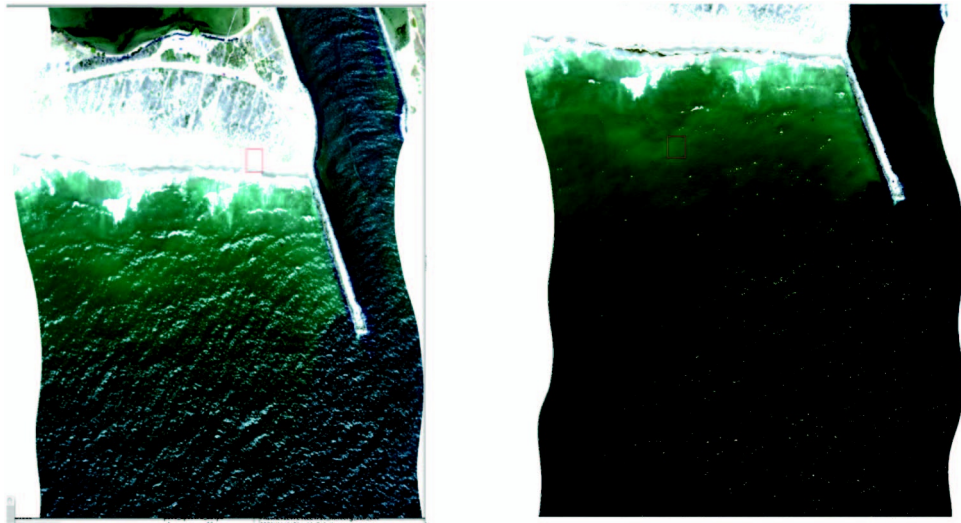
Fig. 28. Example of PRISM RGB image before (left) and after (right) sun glint effect corrections.

Because the solar radiation in the sun-surface-sensor path is affected by absorption and scattering effects from atmospheric gases and aerosols, accurate modeling of these effects is required in order to derive land surface reflectance and water-leaving reflectance spectra from PRISM data. Preliminary atmospheric correction to PRISM data is made using an updated version of ATREM code [39]. First, we corrected for Rayleigh scattering effects and absorption effects from atmospheric gases. In some cases,
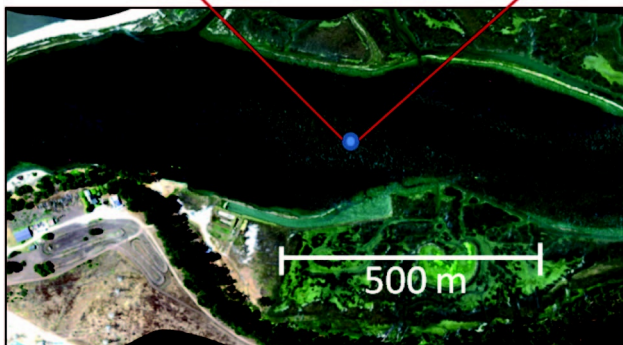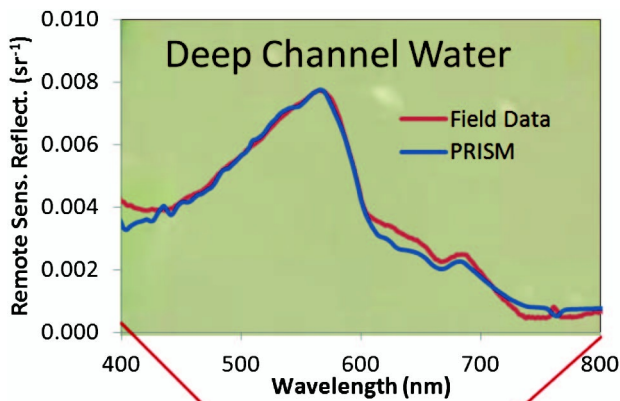

Fig. 29. PRISM-derived reflectance compared to mean of four ASD Field Spec Pro field measurements made during PRISM overflight, for optically deep location in Elkhorn Slough. Field sampling location shown in inset.

the resulting surface reflectance spectra and high-spatial-resolution images over water areas still contain obvious sun glint effects as well as the effects from thin clouds. In order to remove these residual effects, we developed a land/water mask using PRISM channels centered near 660 and 860 nm. For each water pixel, we assumed that the sun glint effect is spectrally constant and equal to the Rayleigh-corrected reflectance value for a channel centered near 980 nm (where the water-leaving reflectance is close to zero). This constant value is subtracted out from all channels in the Rayleigh-corrected reflectance spectrum. The empirical procedure is very effective in removing the sun glint effects, as demonstrated in the right plot of Fig. 28. We note, however, that the effect of sun glint negated the black pixel assumption for the use of the SWIR radiometer as an aid to the atmospheric correction in this case. The SWIR radiometer would have to prove its utility in higher altitude flights, where the effect of sun glint can be averaged over many waves and predicted from wind speed models, and/or on calm days with low sun angle.

Comparison of Rrs derived from the atmospherically corrected imagery and from field measurements over the deep portions of the Elkhorn Slough Channel showed good agreement across the visible spectrum (Fig. 29). Both Rrs spectra peak in green wavelengths (~570 nm), indicating the presence of blue-absorbing sediments, colored dissolved organic matter, and phytoplankton. A chlorophyll fluorescence peak is observed at 685 nm in both spectra as well. This close comparison demonstrates the success of both the atmospheric correction methods and the accuracy of the integrated PRISM system for collecting high-quality data.

7. Conclusions

A wide range of science and application objectives exist for the Earth's coastal water regions. Spectroscopic measurements in the range from 350 to

1050 nm record the absorption and scattering signatures of both in water and shallow benthic constituents. Spectroscopic imaging provides an efficient basis to pursue these objectives while complementing and expanding the limited *in situ* capabilities and resources. However, the low signal and large atmospheric correction create special challenges for remote sensing instruments focused on the coastal ocean. PRISM has combined a range of technologies that are demonstrated for the first time, to the best of our knowledge, in an operational sensor in order to achieve its unique properties and high performance in terms of SNR, response uniformity, polarization, dynamic range, and recovery of high-quality spectra. PRISM uses the Dyson imaging spectrometer design form in conjunction with a set of new technologies to address these challenges. The optically fast Dyson design enables high SNR and outstanding uniformity. The shaped-groove, concave diffraction grating provides low polarization sensitivity and broad spectral coverage. The electron-beam-lithography slit with black silicon provides excellent uniformity and low scattered light. The wide FOV two-mirror reflective telescope supports high throughput and low polarization sensitivity. These technologies have been brought together for the first time in the PRISM instrument.

Following development, PRISM was extensively characterized and calibrated in the laboratory. Specific spectral, radiometric, spatial, and uniformity data sets were acquired and analyzed, and the results are reported in the sections above. Based on these laboratory measurements, PRISM was shown to meet or exceed all of the baseline measurement requirements.

The true test of any remote sensing instrument is acquisition and validation of the measurement characteristics in the flight environment. In May 2012 a set of airborne engineering test flights were organized with PRISM install in a Twin Otter aircraft. The initial engineering test flight over a calibration target on Ivanpah Dry Lake, California, tested the radiometric, spectral, and spatial characteristics of the PRISM instrument in the airborne environment. Comparison of radiance predicted from PRISM calibration data, as measured in the laboratory and constrained by radiative transfer code, with *in situ* measurements of the calibration target showed that PRISM achieved the desired radiometric and spectral performance characteristics. The ability of PRISM to measure fine spatial scales was also demonstrated at the 30 cm (1′) scale with spatial targets deployed at Ivanpah. Engineering test flights were then extended to a dark water target with acquisition of data over Lake Tahoe, California, from the Twin Otter aircraft. The Tahoe data sets demonstrated the wide dynamic range as well as the orthorectification postprocessing capability of data sets collected in the airborne environment for the PRISM system. Along-track summing with orthorectification is key to the high SNR of PRISM.

Following these engineering flights PRISM was returned to the laboratory while the data were assessed and minor instrument system refinements were implemented. In July 2012 a science validation campaign was orchestrated in the Monterey Bay region of California. A comprehensive set of coastal water ground measurements was acquired in concert with the PRISM measurement. The ATREM atmospheric correction code was successfully used to correct the calibrated PRISM measurements, and a sun glint algorithm was successfully demonstrated. A pixel-based sun glint algorithm is required, given the fine spatial sampling of PRISM in the complex coastal environment. This science validation experiment confirmed that PRISM instrument measurements are appropriate for coastal water science and application objectives that require constituent measurement and process monitoring over extended areas. These and all PRISM data are made available to the public [40] in accordance with NASA policies. The PRISM instrument is available for use to the ocean science community through the NASA opportunities.

References

1. H. M. Dierssen, R. C. Zimmerman, R. A. Leathers, T. V. Downes, and C. O. Davis, "Ocean colour remote sensing of seagrass and bathymetry in the Bahamas Banks by high resolution airborne imagery," Limnol. Oceanogr. **48**, 444–455 (2003).
2. J. P. Ryan, H. M. Dierssen, R. M. Kudela, C. A. Scholin, K. S. Johnson, J. M. Sullivan, A. M. Fischer, E. V. Rienecker, P. R. McEnaney, and F. P. Chavez, "Coastal ocean physics and red tides: an example from Monterey Bay, California," Oceanography **18**, 246–255 (2005).
3. H. M. Dierssen, R. C. Zimmerman, D. Burdige, and L. Drake, "Benthic ecology from space: optics and net primary production in seagrass and benthic algae across the Great Bahama Bank," Mar. Ecol. Prog. Ser. **411**, 1–15 (2010).

4. X. Xiong, K. Chiang, J. Esposito, B. Guenther, and W. Barnes, "MODIS on-orbit calibration and characterization," Metrologia **40**, S89–S92 (2003).

5. G. Lin, R. E. Wolfeb, and M. Nishihama, "NPP VIIRS geometric performance status," Proc. SPIE **8153**, 81531V (2011).

6. P. J. Curran and C. M. Steele, "MERIS: the re-branding of an ocean sensor," Int. J. Remote Sens. **26**, 1781–1798 (2005).

7. R. L. Lucke, M. Corson, N. R. McGlothlin, S. D. Butcher, D. L. Wood, D. R. Korwan, R. R. Li, W. A. Snyder, C. O. Davis, and D. T. Chen, "Hyperspectral imager for the coastal ocean: instrument description and first images," Appl. Opt. **50**, 1501–1516 (2011).

8. C. O. Davis, J. Bowles, R. A. Leathers, D. Korwan, T. V. Downes, W. A. Snyder, W. J. Rhea, W. Chen, J. Fisher, W. P. Bissett, and R. A. Reisse, "Ocean PHILLS hyperspectral imager: design, characterization, and calibration," Opt. Express **10**, 210–221 (2002).

9. D. D. Kohler, W. P. Bissett, R. G. Steward, M. Kadiwala, and R. Banfield, "Hyperspectral remote sensing of the coastal environment," in *Hyperspectral Imaging and Sounding of the Environment (HISE)*, OSA Technical Digest (Optical Society of America, 2007), paper JWA19.

10. R. O. Green, M. L. Eastwood, C. M. Sarture, T. G. Chrien, M. Aronsson, B. J. Chippendale, J. A. Faust, B. E. Pavri, C. J. Chovit, M. Solis, M. R. Olah, and O. Williams, "Imaging spectroscopy and the airborne visible/infrared imaging spectrometer (AVIRIS)," Remote Sens. Environ. **65**, 227–248 (1998).

11. C. Simi, E. Reith, and F. Olchowski, "The mapping reflected-energy sensor-MaRS: a new level of hyperspectral technology," Proc. SPIE **7457**, 745703 (2009).

12. P. D'Odorico, E. Alberti, and M. E. Schaepman, "In-flight spectral performance monitoring of the Airborne Prism Experiment," Appl. Opt. **49**, 3082–3091 (2010).

13. P. Mouroulis, R. O. Green, and T. G. Chrien, "Design of push-broom imaging spectrometers for optimum recovery of spectroscopic and spatial information," Appl. Opt. **39**, 2210–2220 (2000).

14. J. Nieke, D. Schläpfer, F. Dell'Endice, J. Brazile, and K. I. Itten, "Uniformity of imaging spectrometry data products," IEEE Trans. Geosci. Remote Sens. **46**, 3326–3336 (2008).

15. D. Lobb, N. Fox, M. Rast, P. Slater, and A. Wilson, "Strategies for calibration of high-resolution imaging spectrometer data," Proc. SPIE **2957**, 287–298 (1997).

16. G. Meister, E. J. Kwiatkowska, B. A. Franz, F. S. Patt, G. C. Feldman, and C. R. McClain, "Moderate-resolution image spectroradiometer ocean color polarization correction," Appl. Opt. **44**, 5524–5535 (2005).

17. G. Meister and B. A. Franz, "Radiometric quality of the MODIS bands at 667 and 678 nm," Proc. SPIE **8153**, 81531M (2011).

18. G. Baudin, G. Maurel, P. Nicol, B. Breault, and G. Peterson, "Medium resolution imaging spectrometer (MERIS): stray light design," Proc. SPIE **2864**, 313–321 (1996).

19. E. Waluschka, S.-Y. Qiu, and G. D. Godden, "MODIS stray light simulation," Proc. SPIE. **2864**, 350–360 (1996).

20. P. Mouroulis, R. O. Green, and D. W. Wilson, "Optical design of a coastal ocean imaging spectrometer," Opt. Express **16**, 9087–9095 (2008).

21. W. Shi and M. Wang, "An assessment of the black ocean pixel assumption for MODIS SWIR bands," Remote Sens. Environ. **113**, 1587–1597 (2009).

22. B. Van Gorp, P. Mouroulis, D. W. Wilson, and K. Balasubramanian, "Polarization and stray light considerations for the Portable Remote Imaging Spectrometer (PRISM)," Proc. SPIE **7812**, 78120R (2010).

23. L. Mertz, "Concentric spectrographs," Appl. Opt. **16**, 3122–3124 (1977).

24. D. W. Wilson, P. D. Maker, R. E. Muller, P. Mouroulis, and J. Backlund, "Recent advances in blazed grating fabrication by electron-beam lithography," Proc. SPIE **5173**, 115–126 (2003).

25. E. Urquiza, C. Vasquez, J. Rodriguez, and B. Van Gorp, "Development and testing of an innovative two-arm focal-plane thermal strap," presented at the Space Cryogenics Workshop, Coeur D'Alene, Idaho, June 2011.

26. Y. Bai, J. Bajaj, J. W. Beletic, M. C. Farris, A. Joshi, S. Lauxtermann, A. Petersen, and G. Williams, "Teledyne imaging sensors: silicon CMOS imaging technologies for x-ray, UV, visible and near infrared," Proc. SPIE **7021**, 702102 (2008).

27. G. Meister, C. R. McClain, Z. Ahmad, S. W. Bailey, R. A. Barnes, S. Brown, R. E. Eplee, B. Franz, A. Holmes, W. B. Monosmith, F. S. Patt, R. P. Stumpf, K. R. Turpie, and P. J. Werdell, "Requirements for an advanced ocean radiometer," NASA TM-2011-215883 (2011).

28. R. O. Green, "Spectral calibration requirement for Earth-looking imaging spectrometers in the solar-reflected spectrum," Appl. Opt. **37**, 683–690 (1998).

29. B.-C. Gao, K. B. Heidebrecht, and A. F. H. Goetz, "Derivation of scaled surface reflectances from AVIRIS data," Remote Sens. Environ. **44**, 165–178 (1993).

30. T. Skauli, "An upper-bound metric for characterizing spectral and spatial coregistration errors in spectral imaging," Opt. Express **20**, 918–933 (2012).

31. H. R. Gordon, T. Du, and T. Zhang, "Atmospheric correction of ocean color sensors: analysis of the effects of residual instrument polarization sensitivity," Appl. Opt. **36**, 6938–6948 (1997).

32. E. Waluschka, "MODIS polarization measurements and simulation and the 4θ effect," Proc. SPIE **3121**, 278–287 (1997).

33. A. Berk, L. S. Bernstein, and D. C. Robertson, "MODTRAN: a moderate resolution model for LOWTRAN 7," Final Report GL-TR-0122 (Air Force Geophysics Laboratory (AFGL), Hanscomb AFB, Massachusetts, 1989).

34. G. P. Anderson, J. Wang, and J. Chetwynd, "MODTRAN3: an update and recent validations against airborne high resolution interferometer measurements," in *Summaries of the Fifth Annual JPL Airborne Earth Science Workshop*, R. O. Green, ed. (JPL Pub., 1995).

35. Y. Zong, S. W. Brown, B. C. Johnson, K. R. Lykke, and Y. Ohno, "Simple spectral stray light correction method for array spectroradiometers," Appl. Opt. **45**, 1111–1119 (2006).

36. P. Mouroulis, B. Van Gorp, R. O. Green, M. Eastwood, J. Boardman, B. S. Richardson, J. I. Rodriguez, E. Urquiza, B. D. Franklin, and B.-C. Gao, "Portable remote imaging spectrometer (PRISM): laboratory and field calibration," Proc. SPIE **8515**, 85150F (2012).

37. S. Adler-Golden, A. Berk, L. S. Bernstein, S. Richtsmeier, P. K. Acharya, M. W. Matthew, G. P. Anderson, C. L. Allred, L. S. Jeong, and J. H. Chetwynd, "FLAASH, A MODTRAN4 atmospheric correction package for hyperspectral data retrievals and simulations," in *Summaries of the Seventh JPL Airborne Earth Science Workshop*, R. O. Green, ed. (JPL Pub., 1998), pp. 9–14.

38. H. M. Dierssen and K. Randolph, "Remote sensing of ocean color," in *Encyclopedia of Sustainability Science and Technology* (Springer-Verlag, 2013).

39. B.-C. Gao and C. O. Davis, "Development of a line-by-line-based atmosphere removal algorithm for airborne and spaceborne imaging spectrometers," Proc. SPIE **3118**, 132–141 (1997).

40. http://prism.jpl.nasa.gov.